PCCP

ROYAL SOCIETY OF CHEMISTRY

PAPER

View Article Online
View Journal | View Issue

Cite this: *Phys. Chem. Chem. Phys.*, 2025, **27**, 2958

Stack bonding in pentacene and its derivatives†

Craig A. Bayse

Received 15th October 2024,
Accepted 4th January 2025

DOI: 10.1039/d4cp03970j

rsc.li/pccp

Understanding the nature of π-stacking interactions is important to molecular recognition, self-assembly, and organic semiconductors. The stack bond order (SBO) model of π-stacking has shown that the conformations of dimers are found at orientations where the combinations of monomer MOs are overall bonding within the stack. DFT calculations show that parallel displaced minima found on the potential energy surface for the π-stacked dimers of pentacene and perfluoropentacene occur when the dimer MOs are constructed from combinations of monomer MOs with an allowed SBO. An examination of the MOs of π-stacked dimers extracted from X-ray structures of alkynyl derivatives like TIPS-pentacene pack at one or more of the minima expected to show similar MO patterns. The π-stacking variability within these materials can be attributed to a balance between the minima allowed by SBO theory and steric effects within the lattice. The offset orientation of the pentacene cores observed in packing of these materials is attributed to the increased overlap of monomer lobes in the dimer and a reduction in two-orbital-four-electron repulsions. Charge mobility estimated from the frontier MOs of the dimer is related to the MO structure that favors PD conformations.

Introduction

π-Stacking interactions contribute to charge mobility in organic electronic materials (OEMs).[1–7] Pentacene derivatives are utilized in a number of OEMs, including organic light-emitting diodes (OLEDs), organic field-effect transistors (OFETs), and organic solar cells (OSCs).[8,9] However, the herringbone packing of pentacene (**1**) and perfluoropentacene (**2**) lacks π–π interactions, which limits their transport properties.[10] Substitutions with bulky alkynyl substitutions (*i.e.*, **3–7**, Fig. 1A) were included to improve processing and charge mobility within organic electronics derived from these materials. These derivatives pack in π-stacked "brick-and-mortar" arrangements which vary in the face-to-face overlap of the pentacene cores.[10–15]

Various groups have used theoretical approaches to understand the electronic structure of OEMs.[16–18] Our group has introduced the concept of the stack bond order (SBO) as an intuitive molecular-orbital (MO) based means for interpreting the conformational preferences of π-stacking interactions.[19–21] These nonbonded interactions universally prefer parallel-displaced (PD) and twisted (TW) conformations over the fully eclipsed sandwich (S) conformation. The SBO approach explains this preference similarly to the bond order in conventional MO theory. Within a π-stacked dimer, the MOs of monomers A and B of the same irreducible representation combine into additive (+) and subtractive (−) linear combinations (eqn (1) and (2)).

$$\phi e_{irrep}(+) = \phi e^{A}_{irrep} + \phi e^{B}_{irrep} \quad (1)$$

$$\phi e_{irrep}(-) = \phi e^{A}_{irrep} - \phi e^{B}_{irrep} \quad (2)$$

At the fully eclipsed sandwich (S) conformation, these pairs of π-type dimer MOs adopt stack antibonding (SA) character for the (+) linear combination and stack bonding (SB) character for the (−) combination (Fig. 1B). Given that the SBO is defined as the difference in the number of SB and SA-type MOs, the *S* conformation has an SBO of zero, which is interpreted in the same way as a zero bond order in conventional MO theory. Therefore, in analogy to the He dimer, the *S* conformation is predicted by the SBO to be unbound as a repulsive two-orbital-four-electron (2o4e) interaction, where the (+) and (−) linear combinations are well separated energetically (Fig. 1B). Likewise, fully eclipsed π-stacking in any aromatic system would be "forbidden".[21] However, PD of the stack stabilizes the (+) combination because the lobes are able to constructively overlap while the (−) combination destabilizes as the overlap decreases. At the minimum PD point in the benzene dimer, both of these MOs have stack bonding character (nonzero SBO) and are near degenerate such that the interaction between them is no longer repulsive.[19] Therefore, the distortion by PD along the slip coordinate in formally non-covalent π-stacking interactions occurs to minimize the repulsive nature of the 2o4e interaction.

While the intermonomer mixing of p_π AOs has been assumed to be greatest at *S* due to the eclipsing of the ring

Department of Chemistry and Biochemistry, Old Dominion University, Norfolk, Virginia 23529, USA. E-mail: cbayse@odu.edu

† Electronic supplementary information (ESI) available. See DOI: https://doi.org/10.1039/d4cp03970j

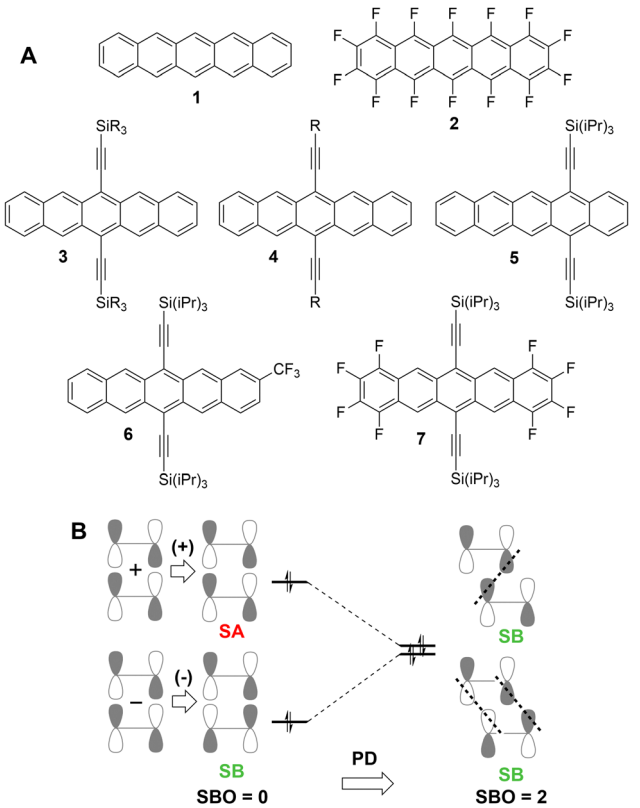

Fig. 1 (A) Pentacene (**1**), perfluoropentacene (**2**), 6,13-TIPS-pentacene (**3**, R = iPr, TIPS = triisopropylsilylethynyl), 6,13-*t*-butylethynylpentacene (**4**, R = *t*Bu) [10], 5,14-TIPS-pentacene (**5**), 4-CF3-6,13-TIPS-pentacene (**6**), octafluoro 6,13-TIPS-pentac TIPS-pentacene (**7**). (B) Example of SBO in a noncovalent π-stacking interaction of a homodimer for a (+) and (−) combination of two monomer π-type MOs. At the *S* conformation, these combinations for stack antibonding (SA) and stack bonding (SB) combinations, respectively (SBO = 0). Parallel displacement shifts the character of the (+)-type MO from SA to SB for a net increase in SBO that increases the interpenetration of the dimer MOs and lowers the interaction energy of the stack by reducing the 2o4e repulsions.

atoms, this applies to the SB-type MOs as the cancelation by the SA-type MOs character depletes the overall inter-ring electron density. PD and/or TW converts one or more dimer MO with SA character at the *S* conformation to SB for a non-zero SBO (Fig. 1B) which increases the overlap between the monomer lobes as well as the inter-ring density, a major component of the dispersion. These conformations also decrease the exchange-repulsion term in the interaction energy[22] which, with the increase in the interpenetration of the electron densities, allows closer stacking of the rings than in the *S* orientation. The most favourable overlap between the p_π-type AOs tends to occur in those conformations that stack similar to graphite-like AB (*i.e.*, Bernal-type[23]) packing.[21] While the favourable overlap may not be evident from the atomic positions in the packing, it can be understood through visual inspection of the MOs in combination with SBO considerations. The number of possible π-stacking conformations increases with the size of the aromatic system as the frontier π-type monomer MOs are divided into more lobes which can form SB-type MOs at varying PD slip distances. The potential for multiple conformations with non-zero SBO is consistent with the polymorphism observed in some polyaromatic hydrocarbons (PAHs).[21] From these observations, a set of stacking bonding rules has been proposed for aromatic homodimers:[21]

(a) Sandwich and other π-stacked conformations that eclipse the ring atoms are forbidden because they have equal numbers of SB- and SA-type dimer MOs (SBO = 0, maximum 2o4e repulsion).

(b) Parallel displaced π-stacked conformations maximize constructive interactions between the monomers because one or more SA-type MO at the *S* conformation will be converted to SB (SBO > 0) to minimize 2o4e repulsions.

(c) Substituted or polyaromatic molecules may have multiple observable π-stacked conformations due to the nodal structure of their extended π-systems.

(d) Twisted conformations are less effective for conversion of SA-type MOs to SB and may be preferred in cases where steric interactions prohibit PD.

In this contribution, the SBO model is used to show how orbital interactions lead to the multiple π-stacking motifs observed in pentacene derivatives. The factors that favor Bernal-type packing are also shown to be linked to MO patterns previously discussed in estimates of the charge mobility.

Methods

Calculations were performed using the Gaussian 09 quantum chemistry package.[24] The M06-2X exchange correlation functional[25] was used with and without Grimme's D3 empirical dispersion correction (M06-2X-D3).[26] These functionals give interaction energies of comparable accuracy to modern advanced functionals for noncovalent dimer test sets.[27] See ref. 21 for a more detailed explanation of the choice of functional for these calculations. The basis sets were triple-ζ quality with polarization functions on all atoms.[28] An 'ultrafine' grid was used for all calculations. Relative energies are not corrected for basis set superposition error (BSSE) because the goal of the study is to compare trends in π-stacking interactions, noting that a previous study of coronene dimers demonstrated that the shape of the potential energy curve did not change when BSSE was included.[29] Dimer structures and potential energy surfaces were generated with monomers fixed at their optimized structures and held parallel. Full optimization of the PD-OV^{xy} minima either led to a slightly more stable structure (<1.0 kcal mol^{-1}) with minimal distortions from the reported conformation or to a lower energy PD-OV^{xy} conformation. The MOs of these fully optimized structures are not significantly different from those shown below.

Results and discussion

Dimers of pentacene (1_{dimer}) and perfluoropentacene (2_{dimer})

1D and 2D potential energy curves and surfaces for 1_{dimer} and 2_{dimer}. From the previous study of coronene and other large PAHs,[21] two types of PD minima were allowed by the SBO model: those which appear slipped over the bonds of the fused

rings (PD-OB) and those which are slipped over the vertices of the rings (PD-OV, *i.e.*, Bernal-like packing). For the oblong pentacenes **1** and **2**, displacement along only the $R_{x,\mathrm{slip}}$ (long axis of pentacene) or $R_{y,\mathrm{slip}}$ (short axis of pentacene) coordinates gives PD-OB^{x} and PD-OV^{y} conformations, respectively (Fig. 2). Multiple PD-OB^{x} minima in the 1D potential curve are found along the long $R_{x,\mathrm{slip}}$ coordinate at increments of one half-ring distance from the maxima at *S* or eclipsed (*E*) conformations (Fig. 3 and Table 1). These minima occur at similar $R_{x,\mathrm{slip}}$ distances to the PD-OB^{x} minima of coronene and other PAHs.[21] One PD-OV^{y} minimum is found at an $R_{y,\mathrm{slip}}$ distance of roughly half the distance to travel across the ring, consistent with minima for the benzene and the lowest energy PAH dimer conformations.[19–21] Each of these conformations corresponds to a minimum in the inter-ring distance R_{vert}.

Variation along both $R_{x,\mathrm{slip}}$ and $R_{y,\mathrm{slip}}$ coordinates generates one type of PD-OB^{xy} and two types of PD-OV^{xy} π-stacking motifs (Fig. 2). PD-OV$_{\mathrm{I}}^{xy}$ conformations orient the 2-carbon over the center of a ring of the other monomer and occur when one unit slips half the diameter of the ring in the $R_{y,\mathrm{slip}}$ direction (∼1.4 Å) and increments of n + 0.5 ring distances in the $R_{x,\mathrm{slip}}$ direction. PD-OV$_{\mathrm{II}}^{xy}$ conformations place the 2-carbon over a tertiary carbon of a fused ring and occur when one unit slips by one C–C bond length in the $R_{y,\mathrm{slip}}$ direction and n ring distances in the $R_{x,\mathrm{slip}}$ direction. These conformations are consistent with Bernal-type stacking and analogous to the two PD-OV^{xy} conformations previously discussed for PAHs.[21] PD-OB^{xy} conformations occur with the slippage of a half-ring distance over the bond from a fully eclipsed conformation (*i.e.*, *S* or *E*-OB^{x}) and were less energetically favorable than those with PD-OV stacking in unsubstituted PAHs.[21] The alkynyl substituted pentacenes adopt various conformations in their brick-and-mortar packing[10] (*e.g.*, **3**, PD-OV$_{\mathrm{IID}}^{xy}$; **4**, PD-OV$_{\mathrm{IIB}}^{xy}$; **5**, PD-OV$_{\mathrm{IA}}^{xy}$; **6**, PD-OV$_{\mathrm{IIC}}^{xy}$; **7**, PD-OV$_{\mathrm{IC}}^{xy}$). A recently synthesized tethered pentacene dimer arranges into the PD-OV$_{\mathrm{IB}}^{xy}$ conformation.[30] Derivatives with substitutions to the pentacene core such as nitriles,[31,32] ethers,[33] thioethers,[34] and thiophenes,[35] as well as tethered anthracenes and substituted hexacenes and heptacenes[36] also stack in similar Bernal-type or PD-OB orientations. Because the π-systems of the alkyne spacers are conjugated with the pentacene core, these groups could potentially participate in stack bonding.

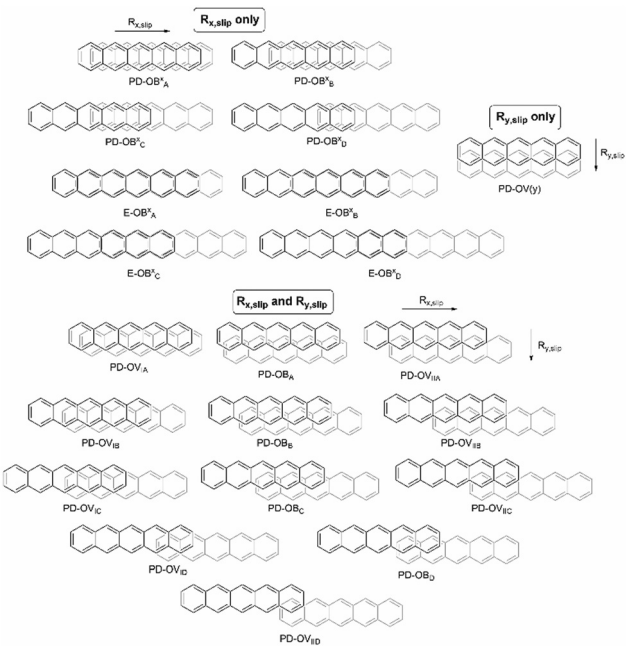

Fig. 2 Possible PD conformations of pentacene-type dimers for translation along the $R_{x,\mathrm{slip}}$-only (PD-OB^{x}), $R_{y,\mathrm{slip}}$-only (PD-OVy), and both $R_{x,\mathrm{slip}}$ and $R_{y,\mathrm{slip}}$ coordinates (PD-OV$_{\mathrm{I}}^{xy}$ and PD-OV$_{\mathrm{II}}^{xy}$). Eclipsed conformations along the over-the-bond $R_{x,\mathrm{slip}}$ coordinate (*E*-OB) are maxima and are predicted to have zero SBO. Not all conformations will necessarily be observed.

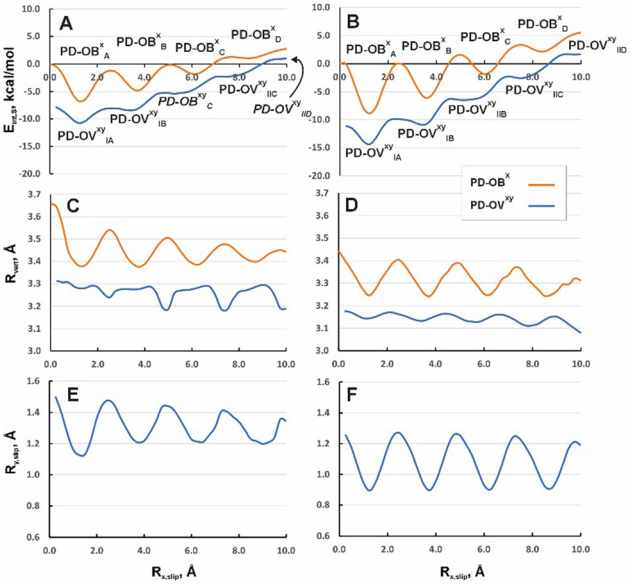

Fig. 3 Potential energy curves with respect to the eclipsed *S* conformation ($E_{\mathrm{int,S}} = E(R_{x,\mathrm{slip}}) - E(S)$) along the $R_{x,\mathrm{slip}}$ coordinate only (PD-OB^{x}, orange) and the $R_{x,\mathrm{slip}}$ coordinate allowing $R_{y,\mathrm{slip}}$ to optimize (PD-OV^{xy}, blue) for **1**$_{\mathbf{dimer}}$ (A) and **2**$_{\mathbf{dimer}}$ (B). Variation in the inter-ring distance R_{vert} for **1**$_{\mathbf{dimer}}$ (C) and **2**$_{\mathbf{dimer}}$ (D). Variation in $R_{y,\mathrm{slip}}$ for **1**$_{\mathbf{dimer}}$ (E) and **2**$_{\mathbf{dimer}}$ (F).

The potential energy surface for simultaneous slipping along both the $R_{x,\mathrm{slip}}$ and $R_{y,\mathrm{slip}}$ coordinates results in more stable minima than the PD-OB^{x} and PD-OV^{y} conformations which appear as saddle points on the 2D surface (Table 1 and Fig. 4). The lowest energy PD-OV$_{\mathrm{IA}}^{xy}$ conformation has the most π-surface overlap of the minima found on the 2D surface. As the stack slips further from the *S* conformation along $R_{x,\mathrm{slip}}$, additional shallow minima appear on the surface with $R_{y,\mathrm{slip}}$ varying between 1.1 and 1.5 Å (0.9–1.3 Å for **2**$_{\mathbf{dimer}}$) and R_{vert} between 3.2 and 3.3 Å (3.1–3.2 Å for **2**$_{\mathbf{dimer}}$) as the dimer adjusts to maximize the interaction between the monomers. These minima are incrementally 3–4 kcal mol^{-1} less stable than PD-OV$_{\mathrm{IA}}^{xy}$ consistent with the decreased overlap between the π-systems. The minima nearest *S* are PD-OV$^{xy}_{\mathrm{I}}$-type conformations; the dimers switch to PD-OV$_{\mathrm{II}}^{xy}$-type once only three of the monomers' fused rings are interacting. The minima occur at similar $R_{x,\mathrm{slip}}$ and $R_{y,\mathrm{slip}}$ distances for **1**$_{\mathbf{dimer}}$ and **2**$_{\mathbf{dimer}}$, but at shorter inter-ring distances for the latter due to the depletion of π-electron density induced by the electron-withdrawing fluorines.

Table 1 DFT(M06-2X) interaction energies E_{int} with and without empirical dispersion corrections calculated relative to separated monomers and, in parentheses, the eclipsed *S* conformation. Values in italics are minima using the default integration grid and are unstable on the larger "ultrafine" grid (see text)

	E_{int} (M06-2X/(TZVP))	R_{vert}, Å	$R_{x,slip}$, Å	$R_{y,slip}$, Å	WBI_{AB}	E_{int} (M06-2X-D3/(TZVP))	R_{vert}, Å	$R_{x,slip}$, Å	$R_{y,slip}$, Å
1_{dimer}									
S	−6.5 (0.0)	3.66	0.00	0.00	0.032	−9.8 (0.0)	3.67	0.00	0.00
PD-OB^{x}_{A}	−13.3 (−6.8)	3.38	1.31	0.00	0.164	−16.5 (−6.7)	3.38	1.31	0.00
PD-OB^{x}_{B}	−11.3 (−4.8)	3.38	3.70	0.00	0.126	−14.3 (−4.4)	3.38	3.69	0.00
PD-OB^{x}_{C}	−8.3 (−1.8)	3.39	6.11	0.00	0.083	−10.7 (−0.9)	3.39	6.08	0.00
PD-OB^{x}_{D}	−5.5 (+1.0)	3.32	8.37	0.00	0.049	−7.3 (+2.5)	3.42	8.27	0.00
PD-OV^{y}	−14.1 (−7.6)	3.32	0.00	1.56	0.078	−17.2 (−7.4)	3.33	0.00	1.54
PD-OV^{xy}_{IA}	−17.3 (−10.8)	3.28	1.25	1.27	0.157	−20 (−10.5)	3.28	1.12	1.27
PD-OV^{xy}_{IB}	−14.9 (−8.4)	3.27	3.46	1.17	0.121	−17.8 (−8.0)	3.27	3.45	1.17
PD-OB^{xy}_{C}	*−11.8 (−5.3)*	*3.27*	*5.50*	*1.36*	*0.089*	*−14.4 (−4.4)*	*3.27*	*5.45*	*1.37*
PD-OV^{xy}_{IIC}	−9.0 (−2.4)	3.22	7.41	1.43	0.078	−10.8 (−1.0)	3.19	7.29	1.40
PD-OV^{xy}_{IID}	*−5.6 (+0.9)*	*3.19*	*9.78*	*1.36*	*0.055*	—	—	—	—
2_{dimer}									
S	−11.9 (0.0)	3.44	0.00	0.00	0.084	−15.7 (0.0)	3.45	0.00	0.00
PD-OB^{x}_{A}	−20.9 (−9.0)	3.24	1.23	0.00	0.230	−24.6 (−8.9)	3.24	1.23	0.00
PD-OB^{x}_{B}	−18.2 (−6.3)	3.23	3.63	0.00	0.176	−21.6 (−5.9)	3.23	3.61	0.00
PD-OB^{x}_{C}	−14.0 (−2.1)	3.24	6.03	0.00	0.122	−16.8 (−1.1)	3.25	6.01	0.00
PD-OB^{x}_{D}	−9.8 (+2.1)	3.26	8.39	0.00	0.075	−12.3 (+3.4)	3.26	8.32	0.00
PD-OV^{y}	−22.9 (−11.0)	3.18	0.00	1.29	0.165	−26.6 (−10.9)	3.18	0.00	1.29
PD-OV^{xy}_{IA}	−26.3 (−14.4)	3.14	1.19	0.90	0.248	−29.9 (−14.2)	3.15	1.19	0.89
PD-OV^{xy}_{IB}	−22.8 (−10.9)	3.13	3.44	0.96	0.148	−26.2 (−10.5)	3.14	3.42	0.96
PD-OV^{xy}_{IIB}	−18.4 (−6.5)	3.14	5.11	1.23	0.130	−21.5 (−5.7)	3.15	5.02	1.25
PD-OV^{xy}_{IIC}	−14.5 (−2.6)	3.12	7.50	1.23	0.105	−16.9 (−1.1)	3.13	7.44	1.23
PD-OV^{xy}_{IID}	−10.3 (+1.6)	3.9	9.81	1.21	0.082	−12.1 (+3.7)	3.10	9.74	1.21

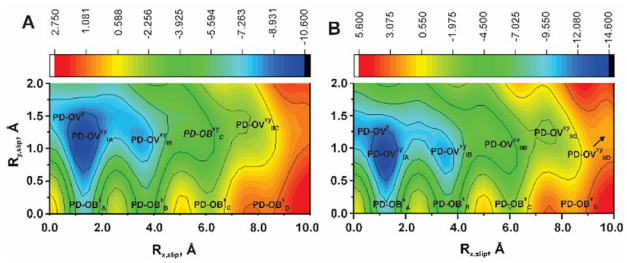

Fig. 4 Potential energy surfaces for parallel-displaced (PD) along both the $R_{x,slip}$ and $R_{x,slip}$ coordinates for **1_{dimer}** (A) and **2_{dimer}** (B). The monomer structures are fixed in this PES. Full optimization of the minima either leads to minimal distortion from the fixed dimer and a slightly lower E_{int} (<1.0 kcal mol^{-1}) or a lower energy conformation.

The minima listed in Table 1 are 2–4 kcal mol^{-1} more stable relative to separate monomers when the D3 empirical dispersion correction is included.[26] The PD-OV^{xy}_{IIB} and PD-OV^{xy}_{IID} conformations are only found for **2_{dimer}** where the E_{int} are generally stronger than for **1_{dimer}**. In addition, the interactions are sensitive to the number of integration lattice points and the inclusion of the D3 empirical dispersion correction. Use of the default grid settings in Gaussian09 finds these conformations as minima where they appear as shoulders on the PES when grids with more integration points are used. The PD-OV^{xy}_{IID} conformation of **1** is not a minimum when the D3 empirical dispersion correction is included.

SBO analysis of 1_{dimer}

To understand the influence of orbital interactions on the conformational preferences of **1_{dimer}** and **2_{dimer}**, the frontier bands of dimer MOs were inspected along each of the 1D and 2D PD coordinates. Minima along each coordinate are consistent with the conversion of at least one (+)-type dimer MO (eqn (1)) with SA character in the *S* conformation to SB at a PD conformation, as expected by the SBO model. Considerations for favorable MO interactions are simplified by focusing on the occupied frontier MOs. Lower-lying MOs show similar patterns of interconversion between SB and SA as the frontier band along each of the PD coordinates. While these MOs can influence the conformation locations, the frontier MOs are assumed to contribute most significantly to the observed minima in analogy to the Walsh rules.[37,38]

For **1_{dimer}**, mixing of the three monomer frontier MOs (ϕ_{3b2g} HOMO, ϕ_{2au} HOMO−1, ϕ_{3b1g} HOMO−2) was considered. At the *S* conformation, the (+) and (−) linear combinations of these MOs form SA- and SB-type dimer MOs, respectively, which cancel for an SBO of zero (Fig. 5). PD along the dimer short axis ($R_{y,slip}$) converts the ϕ_{3b2g}(+) and ϕ_{2au}(+) dimer MOs to SB at the PD-OV^{y} minimum while ϕ_{3b1g}(+) and the (−)-type MOs remain SB for a net positive SBO. ϕ_{3b2g}(+) has no nodes along the PD coordinate and maintains its SA character along the PD coordinate. These shifts in MO character are similar to the benzene dimer where there is also only one node perpendicular to the PD coordinate.[19]

For the PD-OB^{x} minima along the long axis ($R_{x,slip}$) (Fig. 5), all frontier dimer MOs have SB character only for the lowest-energy PD-OB^{x}_{A} conformation. The next three PD-OB minima each have one SA-type dimer MO (ϕ_{2au}(+), ϕ_{3b2g}(+), and ϕ_{3b2g}(−), resp.) which, with the reduced overall co-facial overlap of the monomer lobes, contributes to higher E_{int} for these conformations. In addition, the equal number of SA and SB MOs (SBO = 0) found

at the E-OB^x_A conformation is consistent with SBO analysis, which predicts that E conformations will be unbound.

In Walsh-like diagrams (Fig. 6), the PD-OB^x minima of $\mathbf{1}_{\mathbf{dimer}}$ generally occur at the crossing point of the $\phi_{3b1g}(+/-)$ MOs. Crossing points occur when the (+) and (−) linear combinations of monomer MOs are overall SB in character and degenerate with no 2o4e repulsions between the dimer MOs, contributing to the minimum in E_{int}. Because the sinusoidal behavior of the dimer ε_{MO}s, where minima correspond to the largest overlap of the monomer MO lobes, depends upon the nodal structure of the monomer MOs (*i.e.*, more nodes lead to shorter wavelengths in the oscillation), the crossing points of different (+)/(−) pairs do not occur at the same $R_{y,slip}$ distances. For example, PD-OB^x_A appears closest to the crossing points of all three (+)/(−) pairs of dimer MOs, but the other minima have at least one MO that is near maximum SA character due to a node along the xz plane (Fig. 5).

PD translation along both $R_{x,slip}$ and $R_{y,slip}$ coordinates (Fig. 5) breaks the xz symmetry plane of the dimer to allow lobes that were inaccessible for mixing in PD-OB^x to combine between monomer MOs. This mixing introduces SB character analogous to that found along the PD-OV^y-coordinate. As a result, the PD-OV^{xy} minimum energy conformations in the 2D

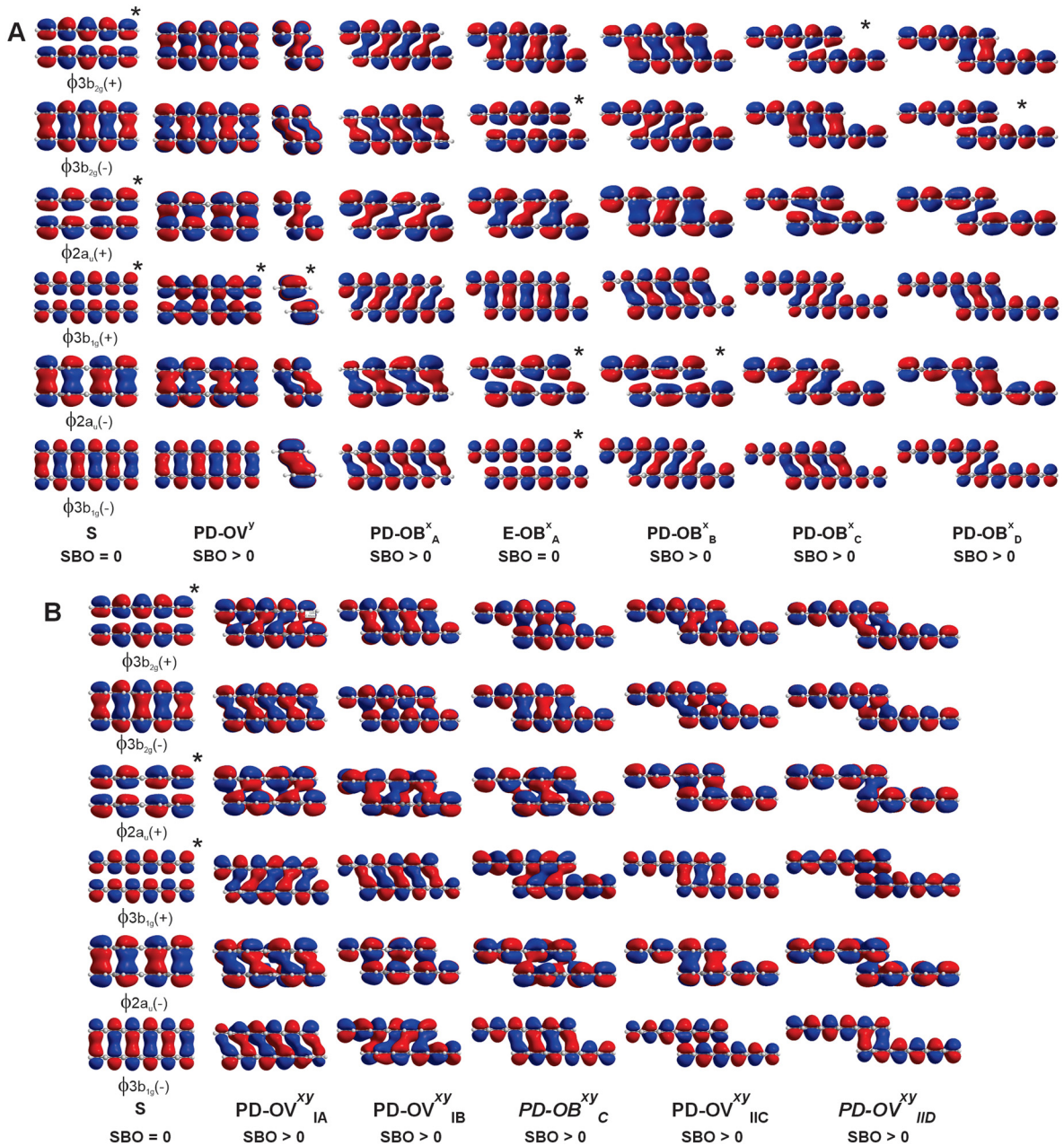

Fig. 5 Frontier dimer MOs for the sandwich (S) and parallel-displaced (PD) conformations of $\mathbf{1}_{\mathbf{dimer}}$: (A) dimer MOs for conformations along the y- and x-slip coordinates (PD-OV^y and PD-OB^x, resp.), (B) dimer MOs for conformations found varying the slip coordinate in both the x- and y-directions (PD-OV^{xy}, PD-OB^{xy}). MOs were plotted with an isosurface value of 0.01 using Chem3D. The frontier MOs for $\mathbf{2}_{\mathbf{dimer}}$ are similar in character and are found in the Fig. S1, ESI.†

PES are located at roughly a half-ring distance slip in the $R_{y,slip}$ direction. These results are consistent with the conformations observed in X-ray structures of substituted pentacenes.[10] These derivatives do not pack with a mirror plane in the pentacene units, a result that was not expected by the synthetic group, but is explained through SBO analysis. The increase in orbital mixing enhances the inter-ring density and favors shorter R_{vert} distances and the stronger E_{int} relative to the PD-OB^x conformations (Table 1). However, not all potential π-stacking conformations (Fig. 2) are found on the PES for $\mathbf{1}_{\mathbf{dimer}}$ due to other contributions to the overall E_{int}.

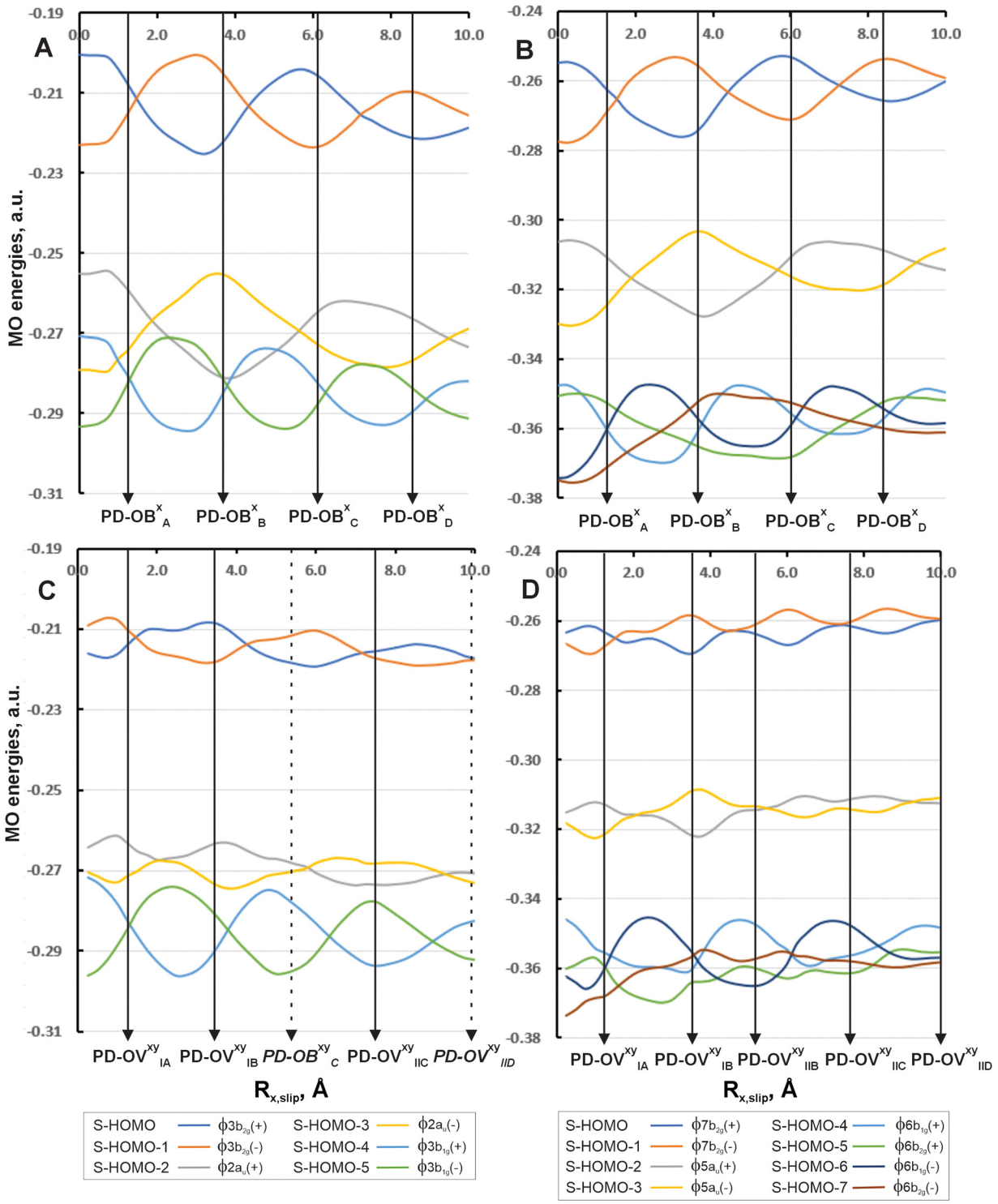

Fig. 6 Walsh-like diagrams for PD along the $R_{x,slip}$ coordinate for the frontier MOs of $\mathbf{1}_{\mathbf{dimer}}$ (A) and $\mathbf{2}_{\mathbf{dimer}}$ (B). Walsh-like diagram for PD along the $R_{x,slip}$ coordinate allowing $R_{y,slip}$ to vary for the frontier MOs of $\mathbf{1}_{\mathbf{dimer}}$ (C) and $\mathbf{2}_{\mathbf{dimer}}$ (D).

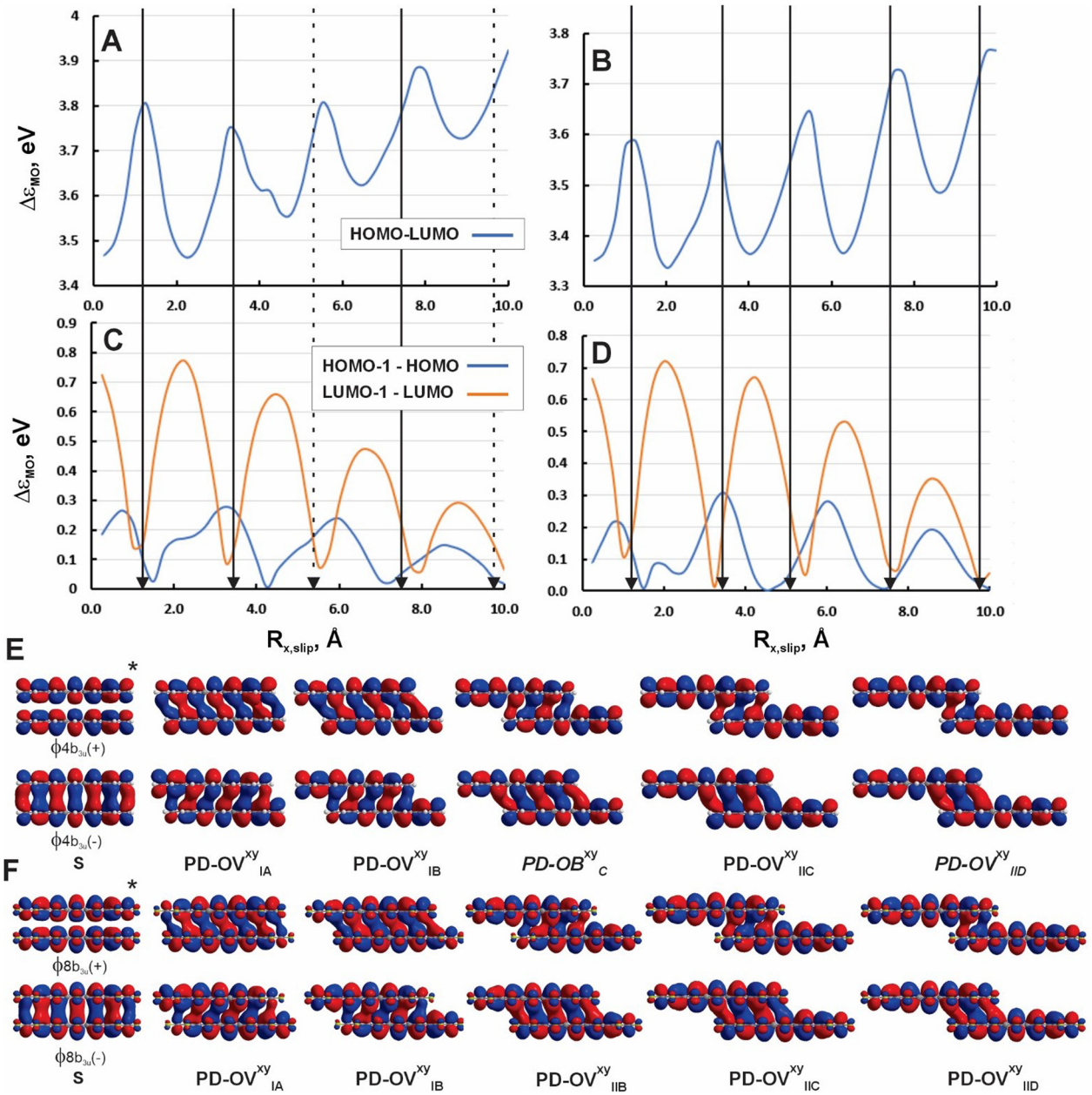

Fig. 7 Trends in the HOMO–LUMO gap of the $\mathbf{1}_{\mathbf{dimer}}$ (A) and $\mathbf{2}_{\mathbf{dimer}}$ (B) dimer along the PD-OV^{xy} coordinate. Minima along the PD-OV^{xy} PES are indicated with vertical arrows (see Fig. 3 and 6). Trends in the estimates of the electron and hole charge mobilities calculated as the ε_{MO} difference ($\Delta\varepsilon_{MO}$) between the HOMO and HOMO−1 and LUMO and LUMO+1 pairs, respectively, of the $\mathbf{1}_{\mathbf{dimer}}$ (C) and $\mathbf{2}_{\mathbf{dimer}}$ (D) dimer over the PD-OV^{xy} coordinate. LUMO and LUMO+1 for the $\mathbf{1}_{\mathbf{dimer}}$ (E) and $\mathbf{2}_{\mathbf{dimer}}$ (F) dimers along the PD-OV^{xy} coordinate. MOs were plotted with an isosurface value of 0.01 using Chem3D.

The mixing of SB character along both PD coordinates complicates the interpretation of the ε_{MO} trends in the PD-OV^{xy} Walsh-type diagrams (Fig. 6). Pairs of dimer MOs maintain the roughly sinusoidal patterns of the PD-OB^{x} MO energies, where the maxima do not necessarily correlate with the least monomer MO overlap due to the mixing of PD-OV^{y} SB character. Irregularities also appear in the patterns due to variations in $R_{y,slip}$ to maximize overlap of the lobes across the xz nodal plane in the monomer MOs. The inflection in the HOMO/HOMO−1 dimer pair near $R_{y,slip}$ = 2.75 Å can be attributed to an PD-OB-like conformation. The more regular behavior of HOMO−4/5 is due to the lack of nodes in the *xz* plane that could limit overlap between the broad monomer lobes.

SBO analysis of $\mathbf{2}_{\mathbf{dimer}}$

The dimer MOs constructed from the four monomer perfluoropentacene frontier MOs were considered in the SBO analysis of $\mathbf{2}_{\mathbf{dimer}}$. The (+)/(−) pairs of the HOMO (ϕ_{7b2g}) and HOMO−1 (ϕ_{5au}) monomer MOs form well-separated individual bands (Fig. 6, Fig. S1, ESI†). Along the PD-OB^{x} and PD-OV^{y} coordinates, these dimer MOs have similar character to $\mathbf{1}_{\mathbf{dimer}}$ with some

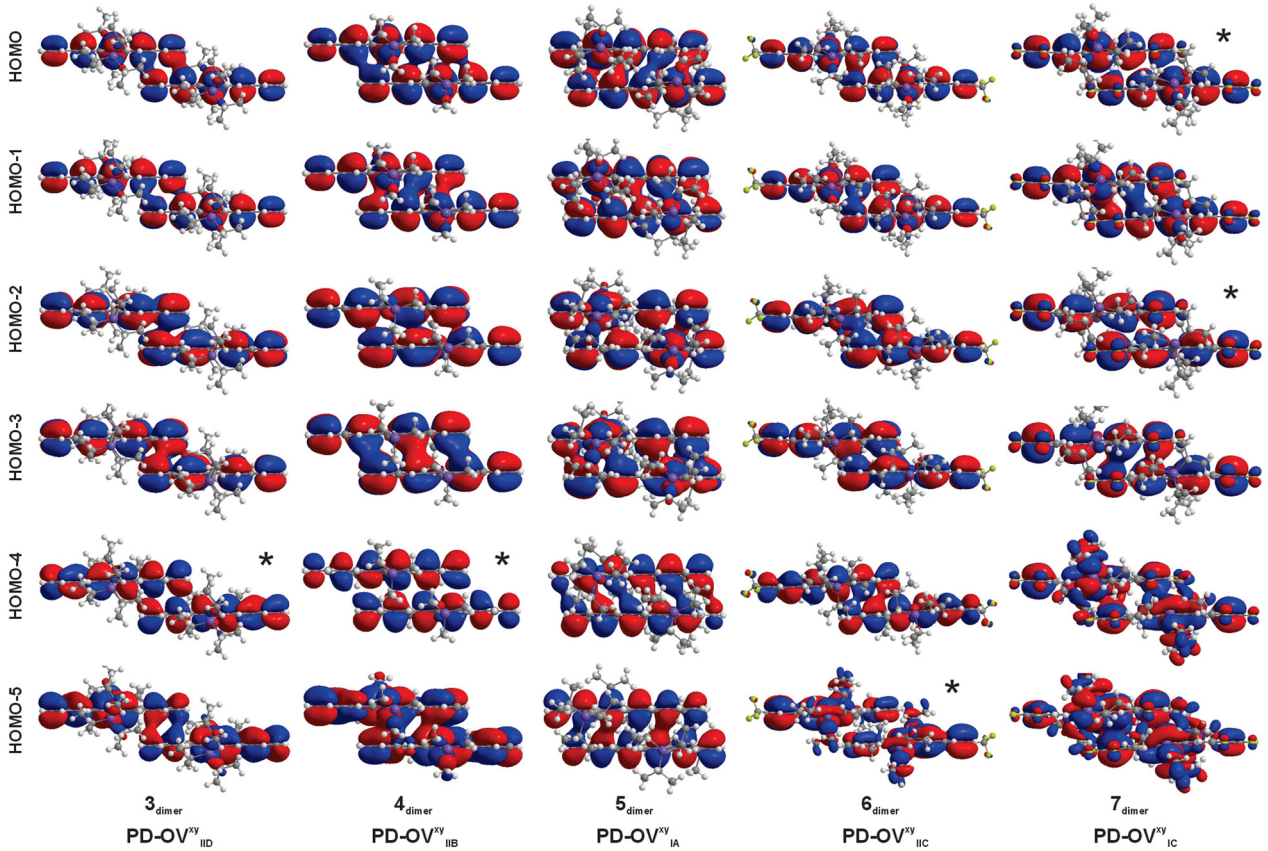

Fig. 8 Frontier MOs for dimer pairs extracted from X-ray crystal structures of π-stacked pentacenes arranged from HOMO (top) to HOMO-5 (bottom). SA MOs are indicated with a (*). The overall SBO for the frontier dimer MOs is greater than zero. MOs were generated from an M06-2X/TZVP single point calculation from the extracted experimental structure and plotted with an isosurface value of 0.01 using Chem3D.

minor mixing of the carbon and fluorine $2p_\pi$ AOs. However, the stabilization of monomer HOMO−2 (ϕ_{6b1g}) by the electron-withdrawing fluorines allows its linear combinations to mix with HOMO−3 (ϕ_{6b2g}) into a band of four dimer MOs. Similar to **1dimer**, only the PD-OB$_A$ minimum along the $R_{x,\mathrm{slip}}$ coordinate has SB character for all frontier dimer MOs with conformations at longer $R_{x,\mathrm{slip}}$ having at least one of the MOs with a node in the xz plane have SA character (PD-OB^x_B: $\phi_{5au}(-)$; PD-OB^x_C: $\phi_{6b2g}(-)$ and $\phi_{7b2g}(+)$; PD-OB^x_D: $\phi_{5au}(+)$, $\phi_{6b2g}(+)$, $\phi_{7b2g}(-)$) to decrease the overall SBO of the respective PD-OB^x conformations.

As for **1dimer**, PD in both $R_{x,\mathrm{slip}}$ and $R_{y,\mathrm{slip}}$ directions allows for the SA-type MOs at the PD-OB^x conformations to mix in the SB character found in the PD-OV^y conformation. The net increase in the overall SBO relative to the PD-OB^x conformations contributes to lower E_{int} and shorter inter-ring distances indicative of increased inter-ring density. Patterns in the Walsh diagram (Fig. 6) are challenging to interpret due to the avoided crossings of the a_g and a_u irreducible representations of the MOs in the lower band. However, most minima occur near the crossing point of the highest two pairs of dimer MOs ((+)/(−)ϕ_{7b2g}(+)/(−)ϕ_{5au}) with PD-OV$^{xy}_{IA}$ shifted closer to the crossing point of (+)ϕ_{6b2g} and (−)ϕ_{6b1g} in the lower band. In contrast, PD-OV$^{xy}_{IB}$ occurs near the crossing point of three MOs in the lower band.

Trends in electronic properties

The most stable energy π-stacked conformations of **1dimer** and **2dimer** are found at the PD conformation closest to S (PD-OV$^{xy}_{IA}$) which has the most overlap between the lobes of the monomer MOs within the dimer. The trends in E_{int} are consistent with the inter-ring electron densities as estimated by the sum of the inter-ring Wiberg bond indices (WBI$_{AB}$, eqn (3) and Table 1).[39]

$$\mathrm{WBI}_{AB} = \sum_{p\in A}\sum_{q\in B}\left(D_{pq}\right)^2 \tag{3}$$

The electron densities are greatest at the first minimum along the PD-OB^x and PD-OV^{xy} coordinates and decreases as fewer monomer lobes are able to mix. As a result, the inter-ring R_{vert} distances at the PD-OV^{xy} minima become significantly shorter than S as a result of the enhanced mixing between monomer MOs. Even though fewer monomer MO lobes can interact at long $R_{x,\mathrm{slip}}$ distances, the R_{vert} distances are similar due to the distance needed for optimal overlap of the carbon p_π lobes.

The trends in charge mobility were estimated along the PD-OV(xy) coordinate as the $\varepsilon_{\mathrm{MO}}$ difference ($\Delta\varepsilon_{\mathrm{MO}}$) for the HOMO and HOMO−1 (electron transfer) and LUMO and LUMO+1 (electron hole) pairs.[40] For the frontier HOMOs, the difference is minimized at the crossing points and maximized when the

pair has maximum SB (HOMO−1) and SA (HOMO) character, (*i.e.*, roughly halfway between the PD-OV^{xy} minima (Fig. 7)). The extent of overlap of monomer MOs is expected to be related to the magnitude of electronic coupling.[1] In $\mathbf{1}_{\mathbf{dimer}}$ and $\mathbf{2}_{\mathbf{dimer}}$, the dimer LUMO and LUMO+1 pair is constructed from the (+)/(−) combinations of the π*-type ϕ_{b3u} MOs which alternate between combinations of SB and SA character. LUMO combinations are generally SB at the minimum energy conformations (Fig. 7). While these unoccupied MOs do not affect the conformation of the π-stack, they influence the electronic properties. This lobal structure of π-systems, previously used to interpret the patterns in the transfer integrals,[40,41] is connected to the structural preferences interpreted through SBO analysis. Minima in the $\Delta\varepsilon_{MO}$ for these unoccupied frontier MOs are also found at the crossing points of the (+) and (−) combinations of the monomer LUMO. Due to the nodal structure of the monomer HOMO and LUMO of $\mathbf{1}_{\mathbf{dimer}}$ and $\mathbf{2}_{\mathbf{dimer}}$, the extrema in $\Delta\varepsilon_{MO}$ occur in different locations with high hole mobility and variable electron mobility at the PD-OV^{xy} minima. The HOMO–LUMO gap is largest near the PD-OV^{xy} minimum structures where LUMO and LUMO+1 are most similar in energy (*i.e.*, when both have SB character and enhanced overlap between the unoccupied monomer MOs).

SBO analysis of substituted pentacenes

For a selection of substituted pentacene derivatives **3–7**, π-stacked dimers were extracted from their X-ray structures and single point calculations were performed to visualize the MOs (Fig. 8). These molecules incorporate alkyne groups with bulky substituents that favor π-stacking between the pentacene cores through various "brick-and-mortar" packing arrangements.[10] The MOs for these extracted dimers are comparable to those found in $\mathbf{1}_{\mathbf{dimer}}$ and $\mathbf{2}_{\mathbf{dimer}}$. Due to the longer inter-ring distance in the X-ray structures (∼3.4 Å *versus* 3.1–3.3 Å in the optimized dimers), some of the MOs do not have effective overlap of lobes, reducing the overall SBO (*i.e.*, HOMO−4 in $\mathbf{3}_{\mathbf{dimer}}$ and $\mathbf{4}_{\mathbf{dimer}}$, HOMO−5 in $\mathbf{6}_{\mathbf{dimer}}$, and HOMO and HOMO−1 in $\mathbf{7}_{\mathbf{dimer}}$). Nonetheless, the overall character is consistent with a non-zero SBO and the interpenetration of the monomer densities. Only in $\mathbf{5}_{\mathbf{dimer}}$ with the most stable PD-OV$_{IA}$ conformation do all dimer MO have SB character. The close overlap of the monomer MOs along with the high electron/hole mobilities determined in Section 2.1.4 may facilitate the rapid quenching of these materials experimentally.[42] Although the distances between the monomers in the X-ray structures are longer than the optimized structures, the dimer MOs are analogous to those of $\mathbf{1}_{\mathbf{dimer}}$ (Fig. 8). Note that optimization of these dimers can result in a different conformation indicating that other factors in the solid state play an important role in the packing orientation in addition to the SBO considerations.

Conclusions

Stack bond order (SBO) analysis is an intuitive means of understanding the conformational preferences and variability in π-stacking motifs.[19–21] The observed packing in various pentacene derivatives can be attributed to the manner in which the monomer MOs combine in dimers. As established by the SBO rules for homodimers,[21] minima of dimers along the $R_{x,slip}$ and $R_{y,slip}$ coordinates are found when the number of MOs classified as SB is greater than the number of SA-type MOs. These minima generally occur where at least one pair of dimer MOs consisting of (+)/(−) pair of linear combinations of monomer MOs is near-degenerate and does not contribute to two-orbital-four-electron repulsions. The offset, graphite-like AB (or Bernal-type) π-stacking[23] observed in alkynyl substituted derivatives is attributed to the greater mixing of monomer lobes when the mirror symmetry of the dimer is broken. The offset π-stacking of TIPS-pentacene and related derivatives was not expected by the synthetic group,[10] but is readily explained by SBO analysis. Given the nodal structure of the frontier monomer MOs, multiple minima are found which are consistent with the variable π-stacking arrangements found in X-ray structures of pentacene derivatives. These conformations occur at similar PD distances to other aromatic systems due to the overlap of p_π-type MOs within the constraints of a non-zero SBO. The patterns in stack bonding character that contribute to favourable π-stacking conformations have also been linked to the charge transport properties of these materials.[40,41] The synergy between the structure and charge transport ensures that π-stacked materials pack in a manner to conducive to acting as an organic semiconductor. Future studies will examine how the SBO can be used to interpret the π-stacking within additional classes of aromatic systems important to organic electronic materials.

Data availability

The data supporting this article have been included as part of the ESI.†

Conflicts of interest

There are no conflicts to declare.

Acknowledgements

Calculations were performed on high performance maintained by ODU Information Technology Services.

Notes and references

1 A. Troisi, *Chem. Soc. Rev.*, 2011, **40**, 2347–2358.
2 A. Pron, P. Gawrys, M. Zagorska, D. Djurado and R. Demadrille, *Chem. Soc. Rev.*, 2010, **39**, 2577–2632.
3 L. Wang, G. Nan, X. Yang, Q. Peng, Q. Li and Z. Shuai, *Chem. Soc. Rev.*, 2010, **39**, 423–434.
4 W. Wu, Y. Liu and D. Zhu, *Chem. Soc. Rev.*, 2010, **39**, 1489–1502.
5 C. Sutton, C. Risko and J.-L. Brédas, *Chem. Mater.*, 2016, **28**, 3–16.
6 O. Ostroverkhova, *Chem. Rev.*, 2016, **116**, 13279–13412.

7 S.-Y. Yang, Y.-K. Qu, L.-S. Liao, Z.-Q. Jiang and S.-T. Lee, *Adv. Mater.*, 2022, **34**, 2104125.
8 J. E. Anthony, *Chem. Rev.*, 2006, **106**, 5028–5048.
9 C. D. Sheraw, T. N. Jackson, D. L. Eaton and J. E. Anthony, *Adv. Mater.*, 2003, **15**, 2009–2011.
10 J. E. Anthony, D. L. Eaton and S. R. Parkin, *Org. Lett.*, 2002, **4**, 15–18.
11 J. E. Anthony, J. S. Brooks, D. L. Eaton and S. R. Parkin, *J. Am. Chem. Soc.*, 2001, **123**, 9482–9483.
12 Y. Shu, Y.-F. Lim, Z. Li, B. Purushothaman, R. Hallani, J. E. Kim, S. R. Parkin, G. G. Malliaras and J. E. Anthony, *Chem. Sci.*, 2011, **2**, 363–368.
13 C. M. S. Combe, D. T. James, J. Wade, A. J. P. White, J.-S. Kim and I. McCulloch, *Tetrahedron Lett.*, 2013, **54**, 6814–6818.
14 S. M. Ryno, C. Risko and J.-L. Brédas, *J. Am. Chem. Soc.*, 2014, **136**, 6421–6427.
15 K. J. Thorley, T. W. Finn, K. Jarolimek, J. E. Anthony and C. Risko, *Chem. Mater.*, 2017, **29**, 2502–2512.
16 D. Beljonne, J. Cornil, L. Muccioli, C. Zannoni, J.-L. Brédas and F. Castet, *Chem. Mater.*, 2011, **23**, 591–609.
17 C. Y. Cheng, J. E. Campbell and G. M. Day, *Chem. Sci.*, 2020, **11**, 4922–4933.
18 V. Bhat, C. P. Callaway and C. Risko, *Chem. Rev.*, 2023, **123**, 7498–7547.
19 P. B. Lutz and C. A. Bayse, *Phys. Chem. Chem. Phys.*, 2013, **15**, 9397–9406.
20 P. B. Lutz and C. A. Bayse, *Int. J. Quantum Chem.*, 2018, **118**, e25513.
21 C. A. Bayse, *Phys. Chem. Chem. Phys.*, 2023, **25**, 20451–20461.
22 J. Henrichsmeyer, M. Thelen, M. Bröckel, M. Fadel, S. Behnle, M. Sekkal-Rahal and R. F. Fink, *Chem. Phys. Chem.*, 2023, **24**, e202300097.
23 J. D. Bernal, Proceedings of the Royal Society of London, Series a Containing Papers of a Mathematical and Physical Character, 1924, vol. 106, pp. 749–773.
24 M. J. Frisch, G. W. Trucks, H. B. Schlegel, G. E. Scuseria, M. A. Robb, J. R. Cheeseman, G. Scalmani, V. Barone, G. A. Petersson, H. Nakatsuji, X. Li, M. Caricato, A. Marenich, J. Bloino, B. G. Janesko, R. Gomperts, B. Mennucci, H. P. Hratchian, J. V. Ortiz, A. F. Izmaylov, J. L. Sonnenberg, D. Williams-Young, F. Ding, F. Lipparini, F. Egidi, J. Goings, B. Peng, A. Petrone, T. Henderson, D. Ranasinghe, V. G. Zakrzewski, J. Gao, N. Rega, G. Zheng, W. Liang, M. Hada, M. Ehara, K. Toyota, R. Fukuda, J. Hasegawa, M. Ishida, T. Nakajima, Y. Honda, O. Kitao, H. Nakai, T. Vreven, K. Throssell, J. A. Montgomery, Jr., J. E. Peralta, F. Ogliaro, M. Bearpark, J. J. Heyd, E. Brothers, K. N. Kudin, V. N. Staroverov, T. Keith, R. Kobayashi, J. Normand, K. Raghavachari, A. Rendell, J. C. Burant, S. S. Iyengar, J. Tomasi, M. Cossi, J. M. Millam, M. Klene, C. Adamo, R. Cammi, J. W. Ochterski, R. L. Martin, K. Morokuma, O. Farkas, J. B. Foresman and D. J. Fox, *Gaussian 09*, Gaussian, Inc., Wallingford, CT, 2009.
25 Y. Zhao and D. G. Truhlar, *Theor. Chem. Acc.*, 2008, **120**, 215–241.
26 S. Grimme, J. Antony, S. Ehrlich and H. Krieg, *J. Chem. Phys.*, 2010, **132**, 154104.
27 N. Mardirossian and M. Head-Gordon, *Mol. Phys.*, 2017, **115**, 2315–2372.
28 A. Schafer, H. Horn and R. Ahlrichs, *J. Chem. Phys.*, 1992, **97**, 2571–2577.
29 Y. Zhao and D. G. Truhlar, *J. Phys. Chem. C*, 2008, **112**, 4061–4067.
30 W. Ishii, M. Fuki, E. M. Bu Ali, S. Sato, B. Parmar, A. Yamauchi, C. H. Mulyadi, M. Uji, S. Medina Rivero, G. Watanabe, J. Clark, Y. Kobori and N. Yanai, *J. Am. Chem. Soc.*, 2024, **146**, 25395–25888.
31 Y.-F. Lim, Y. Shu, S. R. Parkin, J. E. Anthony and G. G. Malliaras, *J. Mater. Chem.*, 2009, **19**, 3049–3056.
32 C. R. Swartz, S. R. Parkin, J. E. Bullock, J. E. Anthony, A. C. Mayer and G. G. Malliaras, *Org. Lett.*, 2005, **7**, 3163–3166.
33 M. M. Payne, J. H. Delcamp, S. R. Parkin and J. E. Anthony, *Org. Lett.*, 2004, **6**, 1609–1612.
34 K. Kobayashi, R. Shimaoka, M. Kawahata, M. Yamanaka and K. Yamaguchi, *Org. Lett.*, 2006, **8**, 2385–2388.
35 M. M. Payne, S. A. Odom, S. R. Parkin and J. E. Anthony, *Org. Lett.*, 2004, **6**, 3325–3328.
36 M. M. Payne, S. R. Parkin and J. E. Anthony, *J. Am. Chem. Soc.*, 2005, **127**, 8028–8029.
37 A. D. Walsh, *J. Chem. Soc.*, 1953, 2260–2266.
38 R. S. Mulliken, *J. Am. Chem. Soc.*, 1955, **77**, 887–891.
39 K. B. Wiberg, *Tetrahedron*, 1968, **24**, 1083–1096.
40 J. L. Brédas, J. P. Calbert, D. A. da Silva Filho and J. Cornil, *Proc. Natl. Acad. Sci. U. S. A.*, 2002, **99**, 5804–5809.
41 A. Troisi, G. Orlandi and J. E. Anthony, *Chem. Mater.*, 2005, **17**, 5024–5031.
42 R. D. Pensack, G. E. Purdum, S. M. Mazza, C. Grieco, J. B. Asbury, J. E. Anthony, Y.-L. Loo and G. D. Scholes, *J. Phys. Chem. C*, 2022, **126**, 9784–9793.